Resolving spectral information from time domain induced polarization data through 2-D inversion

Gianluca Fiandaca,[1,*] James Ramm,[1] Andrew Binley,[2] Aurélie Gazoty,[1]
Anders Vest Christiansen[1,†] and Esben Auken[1]

[1]*Hydrogeophysics Group, Department of Geoscience, Aarhus University, Denmark. E-mail: gianluca.fiandaca@geo.au.dk*
[2]*Lancaster Environment Centre, Lancaster University, United Kingdom*

SUMMARY

Field-based time domain (TD) induced polarization (IP) surveys are usually modelled by taking into account only the integral chargeability, thus disregarding spectral content. Furthermore, the effect of the transmitted waveform is commonly neglected, biasing inversion results. Given these limitations of conventional approaches, a new 2-D inversion algorithm has been developed using the full voltage decay of the IP response, together with an accurate description of the transmitter waveform and receiver transfer function. This allows reconstruction of the spectral information contained in the TD decay series.

The inversion algorithm is based around a 2-D complex conductivity kernel that is computed over a range of frequencies and converted to the TD through a fast Hankel transform. Two key points in the implementation ensure that computation times are minimized. First, the speed of the Jacobian computation, time transformed from frequency domain through the same transformation adopted for the forward response is optimized. Secondly, the reduction of the number of frequencies where the forward response and Jacobian are calculated: cubic splines are used to interpolate the responses to the frequency sampling necessary in the fast Hankel transform. These features, together with parallel computation, ensure inversion times comparable with those of direct current algorithms.

The algorithm has been developed in a laterally constrained inversion scheme, and handles both smooth and layered inversions; the latter being helpful in sedimentary environments, where quasi-layered models often represent the actual geology more accurately than smooth minimum-structure models. In the layered inversion approach, a general method to derive the thickness derivative from the complex conductivity Jacobian is also proposed.

One synthetic example of layered inversion and one field example of smooth inversion show the capability of the algorithm and illustrates a complete uncertainty analysis of the model parameters.

With this new algorithm, *in situ* TD IP measurements give access to the spectral content of the polarization processes, opening up new applications in environmental and hydrogeophysical investigations.

Key words: Inverse theory; Electrical properties; Hydrogeophysics.

INTRODUCTION

Induced polarization (IP) is a geophysical method traditionally used for mineral exploration, which is increasingly applied to environmental investigation. Typical environmental applications include characterization of waste sites (e.g. Weller *et al.* 1999; Aristodemou & Thomas-Betts 2000; Dahlin *et al.* 2002), soil-type discrimination (e.g. Slater & Lesmes 2002; Slater & Reeve 2002; Kemna *et al.* 2004; Gazoty *et al.* 2012) and detection of soil contamination (e.g. Vanhala 1997; Kemna *et al.* 2004; Flores Orozco *et al.* 2012). The importance of spectral content

gained from IP data is increasingly understood, as shown by several recent studies, which correlate the time characteristics of IP to the hydraulic conductivity of soils (e.g. Binley *et al.* 2005; Revil & Florsch 2010; Titov *et al.* 2010).

The IP phenomenon is assumed linear (Shuey & Johnson 1973) and during the last decade it has been widely investigated both in the time and frequency domains, in the laboratory, or through field studies. The TD approach is used considerably more in the field, although spectral information contained in the IP decays is rarely taken into account: the data are typically modelled using the integral chargeability (Oldenburg & Li 1994). Several recent studies assume that TD IP (TDIP) data obey the constant phase angle (CPA) model for the complex resistivity (Van Voorhis *et al.* 1973; Börner *et al.* 1996), and the data are transformed and inverted in frequency domain (FD) (e.g. Slater & Binley 2003; Kemna *et al.* 2004). In both the integral chargeability and CPA approaches effects of the transmitted waveform are neglected, which can have a profound effect on parameter estimation (Tombs 1981; Johnson 1984). Furthermore, spectral content contained within the IP decay is completely disregarded (or potentially erroneously assumed in the CPA approach) as it may only be recovered by considering the full decay during the inversion process.

Other modelling techniques use the entire IP decay instead of the integral chargeability to resolve, for example, the Cole–Cole parameters (Cole & Cole 1941; Pelton *et al.* 1978), but compute the forward response in a two-step process (Yuval & Oldenburg 1997; Hönig & Tezkan 2007). First, the apparent chargeability values are inverted for each time gate independently by means of a 1-D or 2-D direct current (DC) algorithm. Following this, for each layer or cell of the models, the resulting decays are inverted with the TD Cole–Cole model for a homogeneous half-space (the values of the decays for different time gates being obtained from the independent dc inversions).

This approximation works well in a wide range of parameter contrasts (Hördt *et al.* 2006) and the spectral content is retrieved; however, errors may result from neglecting the shape of the transmitter waveform and the receiver transfer function in the modelling process. Furthermore, unrealistic voltage decays may be obtained, as the time-dependent resistivity series calculated in the first step of the inversion process do not necessarily obey the physics of the IP phenomenon, due to differing noise levels and resolution of the independent dc inversions.

Recent advances have resulted in the development of a 1-D laterally constrained inversion (LCI) algorithm (Fiandaca *et al.* 2012), which considers both the whole transmitter waveform and the system transfer function, providing information on the spectral content of IP data in terms of the Cole–Cole parameters on 2-D sections. However, while the 1-D LCI approach works well in quasi-layered environments, like in some sedimentary systems, it may fail in retrieving the geometry of 2-D complex structures.

We have developed a new 2-D inversion approach for modelling TDIP data. Our method builds on the 1-D implementation put forward by Fiandaca *et al.* (2012) and is based around a 2-D complex conductivity kernel (Kemna *et al.* 2000; Kemna *et al.* 2004; Binley & Kemna 2005), which is calculated for a number of frequencies and transformed to the TD using a fast Hankel transform (Johansen & Sørensen 1979). The inversion algorithm has been developed in the LCI framework (Auken & Christiansen 2004; Auken *et al.* 2005; Auken *et al.* 2008; Behroozmand *et al.* 2012; Fiandaca *et al.* 2012). It uses the full IP voltage decay, together with an accurate description of the transmitter waveform and receiver transfer function to retrieve the spectral content of TDIP data in a unique process. One important feature of the LCI inversion scheme is the possibility to invert for both smooth and layered models. For smooth models, the thicknesses of the model layers remain unchanged during the inversion process, whereas for layered models the thicknesses are included in the model space and estimated during inversion. Layered inversion is often superior to smooth inversion in sedimentary environments, where quasi-layered models often represent the actual geology more accurately than smooth minimum-structure models. In such cases, the layered inversion is able to retrieve the depth of the formation boundaries unequivocally, and the uncertainty on the estimated depths can be computed by propagating the data errors through the covariance of the estimator error, as described by Tarantola & Valette (1982). For this reason, both the smooth and the layered approaches have been implemented in the TDIP 2-D LCI algorithm presented in this study.

One synthetic example of layered inversion and one field example of smooth inversion are presented to highlight the different characteristics of the algorithm.

2-D FORWARD RESPONSE

The TD forward response is based around a finite element, FD, complex conductivity 2-D forward response (Binley & Kemna 2005). The forward response is calculated for a number of decades in frequency, as required by the fast Hankel transform (Johansen & Sørensen 1979) for the transform to the TD.

FD FORWARD RESPONSE

The FD forward response adopted in this study assumes an isotropic 2-D distribution of the complex conductivity and neglects electromagnetic induction. Consider the forward problem for the 2-D distribution of the complex conductivity $\sigma^*(x, z, \omega)$ at a given frequency ω (hereafter all complex variables will be indicated by an asterisk superscript). With a point source at the origin with (zero-phase) current I the problem can be defined by Poisson's equation, Fourier transformed in the strike (y) direction (e.g. Weller *et al.* 1996; Binley & Kemna 2005):

$$\frac{\partial}{\partial x}\left(\sigma^*\frac{\partial \phi^*}{\partial x}\right) + \frac{\partial}{\partial z}\left(\sigma^*\frac{\partial \phi^*}{\partial z}\right) - \lambda^2 \phi^* \sigma^* = -I\delta(x)\delta(z), \tag{1}$$

where ϕ^* is the Fourier-transformed complex potential, λ is the Fourier transformation variable for the assumed strike (y) direction and δ represents the Dirac delta function. The differential eq. (1) is solved for Neumann- and Dirichlet-type boundary conditions by using the finite element method, where the continuous complex conductivity function $\sigma^*(x, z, \omega)$ is discretized across a mesh, giving $\sigma_{i,j}^*(\omega)$, where i and j are the indices of the mesh. Once the discrete complex potential distribution is calculated for a set of wavenumbers λ for each current injection position, inverse Fourier transform and appropriate superposition yields the transfer impedance $Z^*\left(\sigma_{i,j}^*(\omega), q_{ABMN}\right)$ for any quadrupole q_{ABMN}.

Definition of the model space

The discrete distribution of the complex conductivity $\boldsymbol{\sigma}^*(\omega) = \left\{\sigma_{i,j}^*(\omega)\right\}$ for the FD response does not constitute the model space of the inversion algorithm presented in this study. Instead, the model space is defined by means of a parametrization of the polarization, for example, the Cole–Cole parametrization as defined by Pelton *et al.* (1978) or the CPA model, as defined by Van Voorhis *et al.* (1973). The complex conductivity of each cell (i, j) of the finite element mesh is therefore computed as a function of both the frequency ω, and the N parameters of the polarization modelling $\boldsymbol{p} = \{p_1, \ldots, p_N\}$, through:

$$\sigma_{i,j}^*(\omega) = f^*\left(\omega, \boldsymbol{p}_{i,j}\right) \tag{2}$$

.

For instance in the case of the Cole–Cole model the parametrization takes the form:

$$f_{\text{Cole–Cole}}^*(\omega, \boldsymbol{p}) = \frac{1}{\rho\left[1 - m_0\left(1 - \frac{1}{1+(i\omega\tau)^c}\right)\right]}, \tag{3}$$

where ρ is the direct current resistivity, m_0 is the intrinsic chargeability as defined in Seigel (1959), τ is the time constant, c is the frequency exponent and i is the imaginary unit.

In the inversion algorithm presented in this study the subsurface is discretized in rectangular blocks. Hereafter the number of model rows is indicated by N_{layers}, while the number of model columns by N_{models} [in analogy with the 1-D layered models of the 1-D–LCI implementation presented by Fiandaca *et al.* (2012)]. Hence the model space $\boldsymbol{m}$ is defined as follows:

$$\boldsymbol{m} = \left\{p_{l,m,n}; \text{thk}_{k,m}\right\}, \tag{4}$$

where $\text{thk}_{k,m}$ represents the thickness of the block (k, m) and the indices vary in the ranges: $l = \left[1, N_{\text{layers}}\right]; m = [1, N_{\text{models}}]; n = \left[1, N_{\text{parameters}}\right]; k = \left[1, N_{\text{layers}} - 1\right]$. In the implementation of the presented inversion scheme it has been decided to treat the finite element forward mesh as an input of the algorithm decoupled from the model discretization. Consequently, each model block can be arbitrarily subdivided into several mesh cells (both vertically and horizontally) to improve the resolution of the forward computation without increasing the size of the model space.

The Cole–Cole model is the most widely used in literature for describing the polarization phenomenon, both in the time and frequency domains, at laboratory scale or in field applications. For this reason, eq. (3) is used for defining the model space in all the examples presented here. Nevertheless, the inversion algorithm is not bound to a unique model parametrization: both the CPA model and the Cole–Davidson model (Davidson & Cole 1951) have been implemented and can be used instead of the Cole–Cole model for inverting data and any other existing parametrization is implementable through eq. (2).

TD transform

Once the model space and the polarization parametrization are defined, and the complex conductivity distribution has been calculated, it is possible to compute the transfer function of the system, $Z^*(\boldsymbol{\sigma}^*(\boldsymbol{m}, \omega), q_{ABMN})$, for any quadrupole q_{ABMN} defined on the forward mesh.

The TD switch-on step response can be computed by the inverse Fourier transform of the kernel $Z^*(\boldsymbol{\sigma}^*(\boldsymbol{m}, \omega), q_{ABMN})/i\omega$, that is, the FD step response. Finally, the TD switch-off step response, V_{STEP}, is computed for an arbitrary quadrupole, q_{ABMN}, and any time, t ($t = 0$ being the turn-off time), by means of the switch-on step response and the dc response, $Z(\boldsymbol{\sigma}(\boldsymbol{m}, \omega = 0), q_{ABMN})$, as follows:

$$V_{\text{STEP}}(t, q_{ABMN}, \boldsymbol{m}) = \begin{cases} Z(\boldsymbol{\sigma}(\boldsymbol{m}, \omega = 0), q_{ABMN}) & t \leq 0 \\ Z(\boldsymbol{\sigma}(\boldsymbol{m}, \omega = 0), q_{ABMN}) - \frac{2}{\pi}\int_0^\infty \text{Im}\left(-\frac{Z^*(\boldsymbol{\sigma}^*(\boldsymbol{m}, \omega), q_{ABMN})}{i\omega}\right)\sin(\omega t)\,d\omega & t > 0 \end{cases} \tag{5}$$

wherethe inverse Fourier transform is expressed with a sine/cosine transform of the imaginary/real part of the kernel (with/without change of sign), because the kernel represents the transfer function of a causal process.

The integration in eq. (5) is implemented in terms of Hankel transforms (Johansen & Sørensen 1979; Effersø *et al.* 1999) and to decrease the computation time $V_{\text{STEP}}(t, q_{ABMN}, \boldsymbol{m})$ is calculated for fixed (log-spaced) values of the variable t. The Hankel filter coefficients can then be saved in tables, reducing the number of kernel computations, while values at the times defining the decays are computed by means of cubic splines.

a) Superposition of Pulses

Actual Response

c) Syscal Pro Filter

b)

d) Filter Effect
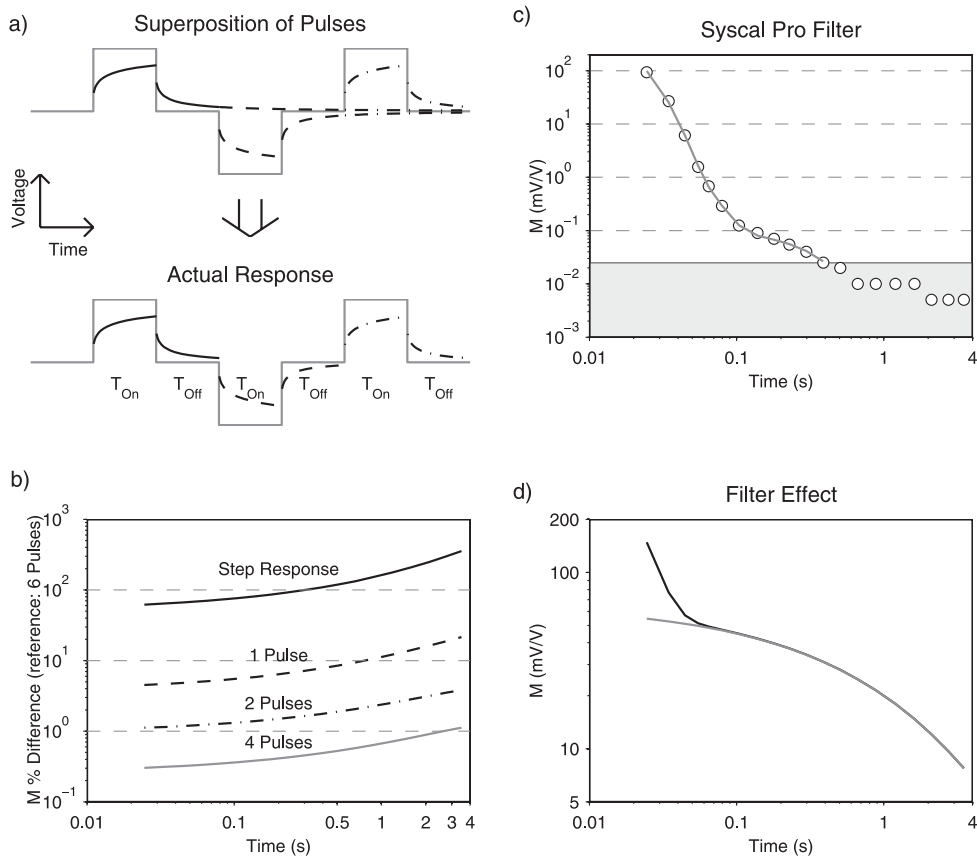
Figure 1. (a) Construction of the pulse response by superimposing two-step responses; (b) IP percentage difference between decays with different number of stacks (a decay stacked six times is used as a reference) for the homogeneous half-space described by the Cole–Cole parameters ($m_0 = $ w 100 mV V^{-1}, $\tau = 2$ s, $c = 0.5$). Solid black line, step response; dashed line, 1 pulse; dotted-dashed line, 2 pulses; grey solid line, 4 pulses. The on- and off-times used for the waveform are: $T_{on} = T_{off} = 4$ s. Note that the per cent axis is logarithmic. (c) IRIS Syscal Pro filter effect (circles) measured in the time domain on a non-chargeable resistor. The grey line represents the modelling of the filter, for which the measurements in the grey rectangle have not been taken into account (because the limit of the digitization of the data has been reached). (d) Example of forward response with the filter implementation (black line) and without the filter implementation (grey line).

MODELLING OF WAVEFORMS AND RECEIVER EFFECTS

Fiandaca *et al.* (2012) addressed the issue of modelling the effects of the current waveform, stacking of measurements and the effect of filters present in dc resistivity and IP instruments. These issues have been implemented in the 2-D code using the same procedures, and a brief summary of the effects detailed in Fiandaca *et al.* (2012) is given here.

The duration of a current pulse transmitted by TDIP equipment is typically less than the time taken for an IP signal to fully decay. This means that the pulse response obtained is actually a superposition of two time-shifted step responses. Due to this, the pulse response has a smaller amplitude and decays faster than a step response. Stacking measurements, which is normal procedure to reduce noise content, can be expressed as a series of superimposed step responses (Fig. 1a). This averages different decays and therefore the number of stacks used for a given measurement can heavily affect the resulting signal. Fiandaca *et al.* (2012) demonstrated that the typical stacked signal can differ from a single step response by 60–400 per cent (Fig. 1b)

The receiver transfer function can also highly influence the measured data. TDIP meters, such as the IRIS Syscal Pro, have a digital filter implemented to reduce noise. This has the unwanted effect of distorting the IP signal at early times (Fig. 1c); these early time data should be rejected without proper modelling of the filter characteristics.

Jacobian computation

The TD forward response F_{TD} is computed through the inverse Fourier transform of the FD response F_{FD}^* (eq. 5) and superposing time-shifted step responses for the implementation of the current waveform (Fiandaca *et al.* 2012), that is, through a linear transformation $L_{\text{time transform}}$. For this reason the differentiation and the Fourier transform commute and the TD Jacobian for the generic parameter p_n, $\frac{\partial F_{TD}}{\partial p_n}$, can be computed by applying the same transformation used for the forward response to the FD Jacobian $\frac{\partial F_{FD}^*}{\partial p_n}$, that is:

$$\left.\frac{\partial F_{TD}}{\partial p_n}\right| := \frac{\partial L_{\text{timetransform}}\left(F_{FD}^*\right)}{\partial p_n} = L_{\text{timetransform}}\left(\frac{\partial F_{FD}^*}{\partial p_n}\right) \tag{6}$$

The FD Jacobian $\frac{\partial F_{\text{FD}}^*}{\partial p_n}$ in eq. (6) is computed from the complex conductivity Jacobian by the chain rule:

$$\frac{\partial F_{\text{FD}}^*}{\partial p_n} = \frac{\partial F_{\text{FD}}^*}{\partial \sigma^*} \cdot \frac{\partial \sigma^*}{\partial p_n}, \tag{7}$$

where $\frac{\partial \sigma^*}{\partial p_n}$ is the partial derivative of eq. (2) for the parameter p_n. The FD complex conductivity Jacobian, $\partial F_{\text{FD}}^*/\partial \sigma^*$, in eq. (7) is computed by the adjoint method, whereby the sensitivity corresponding to a potential, $\phi_{i,k}^*$, at the node i due to a source at node k, is represented as the superposition of potentials, $\phi_{l,i}^*$ at nodes l of the jth element due to a current, I_i, at node i. This is written as:

$$\frac{\partial \phi_{i,k}^*}{\partial \sigma_j^*} = \frac{1}{I_i} \sum_l \sum_m a_{jlm} \phi_{l,i}^* \phi_{m,k}^* \phi_{l,i} \phi_{m,k}, \tag{8}$$

which is the weighted double sum of the complex potentials over all nodes, l,m of the respective element where a_{jlm} is local finite element conductance matrix for the l,mth element.

The layered inversion scheme also requires the derivatives of the forward response with respect to the layer thicknesses. As shown in detail in the Appendix the FD thickness derivatives $J_{\text{FD}}^{\text{thk}*}$ are calculated from the FD complex conductivity Jacobian $\partial F_{\text{FD}}^*/\partial \sigma^*$, through:

$$J_{\text{FD}}^{\text{thk}*} = \frac{\partial F_{\text{FD}}^*}{\partial \text{thk}} \cong \frac{\partial \left(\partial F_{\text{FD}}^*/\partial \sigma^* \right)}{\partial \text{thk}} \cdot \Delta \sigma^*, \tag{9}$$

where $\Delta \sigma^*$ represents the difference of the complex conductivity between the two layers used for the computation of the thickness (thk) derivative. Eq. (9) is exact for infinitesimally small values of $\Delta \sigma^*$, while in practice the error is typically 10–20 per cent, as shown in the next section. Finally, the TD Jacobian with respect to thickness $J_{\text{TD}}^{\text{thk}}$ is obtained applying the same linear transformation used for the forward response.

Optimization and accuracy of the algorithm

Several factors are involved in ensuring minimal computation time of the inversion algorithm, and therefore its applicability:

(1) Fast computation of the TD Jacobian, by using a fast Hankel transform of the FD Jacobian and by avoiding the calculations for low-sensitivity elements.

(2) Both the kernels of the time transform, that is, the FD forward response and Jacobian, can be calculated for a small number of points per frequency decade, while cubic splines are used to interpolate the response to the necessary sampling required for convergence and accuracy of the fast Hankel transform (typically 10 points per decade).

These features, together with use of parallel computing through the open multiprocessing (OpenMP) application programming interface (API), ensure fast computations, with the inversion time being comparable with that of dc algorithms, as shown in the following sections.

Optimization of the Jacobian computation

There can be several million elements in the Jacobian requiring transformation from frequency to TD. For this reason, it is crucial to use a fast algorithm for the Fourier transform. The speed of the Jacobian computation can be increased further by calculating it in parallel in the inversion process and reducing the number of elements to be computed. The reduction is obtained by using the lateral focus (LF) of the quadrupoles, obtained by numerical integration of the 2-D sensitivity distributions for the homogeneous half-space. The Jacobian elements for which the distance between the lateral focus LF of the corresponding quadrupoles and the location of the model parameter exceeds a pre-defined maximum threshold MD are ignored:

$$\frac{\partial F_{\text{TD}}(q_{ABMN})}{\partial p_{l,m,n}} = 0 \quad \forall l, q_{ABMN} | |x_l - \text{LF}(q_{ABMN})| \leq \text{MD}, \tag{10}$$

where x_l represents the position along the profile of the model corresponding to the parameter $p_{l,m,n}$ and the indices l, m, n are defined as in eq. (4).

The threshold MD is an input parameter of the inversion and can be tuned for speed or accuracy. Typically, with MD $\geq$ 10 electrode spacings, reducing the number of elements has negligible effect on accuracy.

SPLINING OF THE FD KERNELS

The FD forward response and Jacobian, that is, the kernels of the Hankel transform, are typically calculated over 13 decades of frequency, between 10^{-3} and 10^{10} Hz. The extent of the frequency range is required for the convergence of the convolution and it is driven by the variability of the Hankel coefficients, more than by the FD kernels. To ensure the accuracy of the Hankel transform, 10 points per decade are required, but the FD kernels are much smoother than the transform coefficients. To further reduce computation time, the FD kernels are only calculated for a small number of points per decade and cubic splines are used to interpolate the response to the 10 points per decade
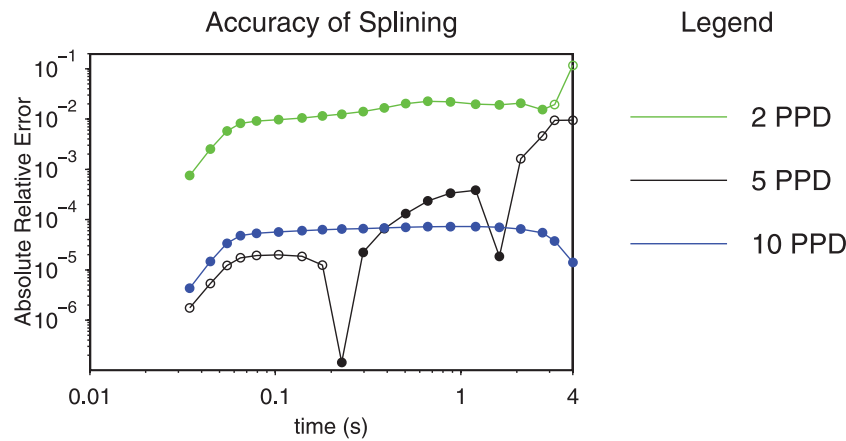
Figure 2. The accuracy of the 2-D time domain forward response by calculating the frequency domain kernel at 2, 5 and 10 points per decade (PPD) and using cubic splines to interpolate the kernel to 10PPD. The reference for the accuracy computation is the 1-D forward response on the quadrupole and the two-layer model shown in Fig. 3(f). Green line: 2 PPD; black line: 5 PPD; blue line: 10 PPD. Empty circles: negative differences with the reference; Full circles: positive differences with the reference. The 2 PPD and 5 PPD plots present abrupt variations where the difference with the reference response changes sign.

as required by the fast Hankel transform. In fact, the interpolation by cubic splines preserves the continuity of the FD kernels and their derivatives and adds negligible computation time to kernel computation. The accuracy of the forward response has been tested by comparing the 2-D forward response with the 1-D response developed in Fiandaca *et al.* (2012) for layered models. Fig. 2 shows the accuracy of using cubic splines for two, five and 10 points per decade when compared to the 1-D response, for the model and the quadrupole described in Fig. 3(f). The accuracy computation of Fig. 2 refers to data expressed in terms of chargeability M. For five points per decade, the relative error is typically less than 1 per cent, which is entirely satisfactory and less than 10 per cent for two points per decade, which is suitable for the first few iterations in the inversion procedure when the error between model and forward response is still expected to be high.

Parameter derivatives for the Jacobian can also be splined; Fig. 3 shows the absolute relative error for each parameter on a two-layer model (Fig. 3f) when using five points per decade, the reference again being the 1-D computations. Also, in Fig. 3 the data for the Jacobian computation are expressed in terms of apparent resistivity ρ_a (dc value) and chargeability M (IP decays), for the quadrupole indicated in Fig. 3(f). The accuracy of the Jacobian with respect to m_0, τ and c (Figs 3b–d) is below 0.1 per cent, while the accuracy with respect to ρ and thickness is below $\sim$10 per cent (Figs 3a and e). The Jacobian elements of the IP decay with respect to ρ are much smaller than the values with respect to the other parameters, which explains the higher relative errors of the last gates of Fig. 3(a). In fact, for homogenous half-spaces the chargeability M is not affected at all by the resistivity ρ, and for inhomogeneous models the dependence of M on ρ is less pronounced than on m_0, τ and c. Consequently the IP elements of the Jacobian with respect to ρ approach zero for late times at a faster rate and the accuracy is lower at the last gates. This effect is also enhanced by the implementation of the current waveform, that requires the summation of several time-shifted step responses for computing the forward response (Fiandaca *et al.* 2012). The higher relative errors of the thickness derivatives (Fig. 3e) are due to the high contrast of the complex conductivity, $\Delta\sigma^*$, between the model layers (eq. 9). In any case, achieving 10 per cent accuracy in the Jacobian is enough to ensure convergence of the inversion, since direction and approximate step size, especially during the first iterations, are sufficient for ensuring convergence of the iterative process.

The FD forward response and Jacobian are computed in parallel over the different frequencies required by the Hankel transform. By calculating the kernels every two points per decade over the 13 decades required in the transform, less than 30 frequencies are needed for the FD computations.

Finally, a 'low resolution' mode has been implemented so that during early iterations, where the misfit between data and model is expected to be large, a coarser mesh may be used for finite element calculations as well as fewer points per decade in frequency and a smaller maximum distance threshold MD. As the misfit becomes smaller, greater accuracy is necessary and a finer mesh is used, along with more of points per decade and a higher MD threshold to improve the accuracy. Table 1 summarizes the computation time of the FD forward response and Jacobian for varying number of points per decade and number of central processing units (CPUs), using the FD single frequency forward and Jacobian computation as reference and the model and data described in the synthetic example of next paragraph (the FD single frequency forward and Jacobian computation has not been parallelized and uses only one CPU). Additionally, the time taken for the time transform is displayed. The use of the FD single frequency forward and Jacobian computation as reference on Table 1 enhances significantly the generality of the results shown in the table itself. In fact, in this way the results are practically independent on the CPU type, on the model, on the data sequence and on the time efficiency of the single frequency computation itself. Furthermore, the forward and Jacobian computation at zero frequency is a dc code, and the numbers in Table 1 can be intended as relative speed compared to a dc code. From the table it can be seen that the overall inversion time of the presented scheme, when working on multi-CPUs servers, is comparable with that of the single frequency computation, that is, of dc algorithms. With 32 CPUs, choosing two points per decade and MD = 10 electrode spacings, gives a
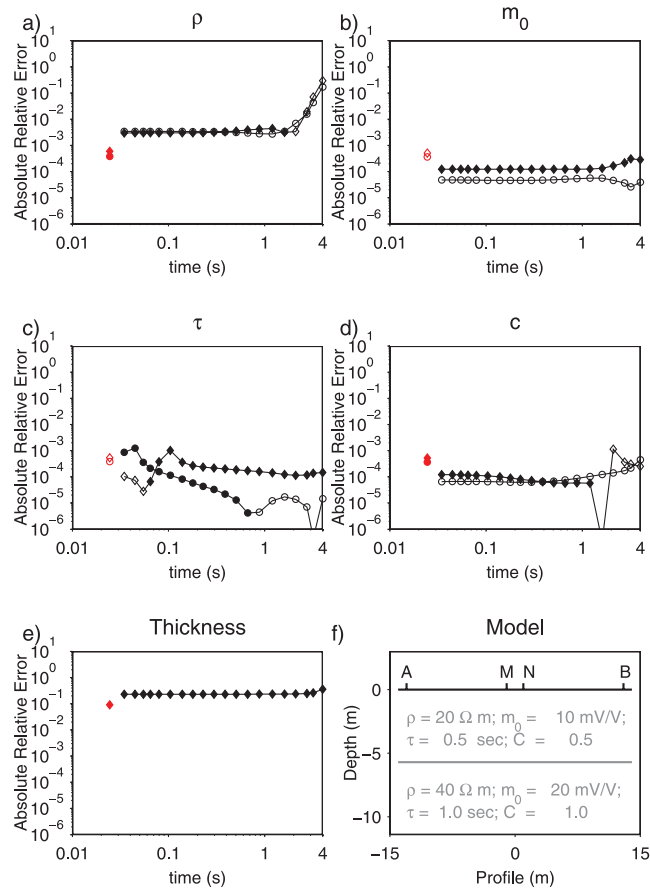
Figure 3. Accuracy of calculating the time domain Jacobian by using 5 points per decade in the frequency domain kernel and interpolating to the required sampling rate with cubic splines. The Jacobian is calculated for the quadrupole and the two-layer model shown in (f) and the reference computations are the 1-D ones; (a–e) show the accuracy in each layer for the Cole–Cole parameters m_0, c, τ, ρ and thickness, respectively. Red circles/diamonds indicate the derivatives of the apparent resistivity and the black circles/diamonds show the derivatives of the apparent chargeability (for 20 time gates) of the first/second layer. Empty markers: negative differences with the reference; full markers: positive differences with the reference.

Table 1. Measurements of computation speed. The single frequency forward and Jacobian computation, whose calculation is not parallelized, is used as reference for the computation speed. Thus, the table entries are expressed in relative values, that is (computation time)/(reference time for 1 CPU). The model and the settings described in the synthetic example of Fig. 4 were used to perform the timing comparison.

	Number of CPUs					
	1	2	4	8	16	32
Forward response and Jacobian 2 points per decade	30	16	8.2	4.3	2.9	1.7
Forward response and Jacobian 5 points per decade	71	37	19	9.7	7.6	4.9
Forward response and Jacobian 10 points per decade	141	73	37	20	10.8	7.8
Time transform of the forward response	0.03	0.02	0.01	0.007	0.004	0.003
Time transform of the Jacobian (MD $= \infty$)	28	20	12	7.1	4	2.5
Time transform of the Jacobian (MD $= 10$ electrode spacings)	7.5	5.3	3.1	1.8	1.0	0.6

computation time only 2.3 times slower than that required for a single frequency forward response (summing the FD computation time and the time transform time). Choosing five points per decade gives a speed 5.5 times slower.

INVERSION PROCESS

The inversion routine used is described in full detail by Auken & Christiansen (2004). The data vector contains all apparent chargeability and resistivity values for all vertical models, quadrupoles and time gates (for chargeability) such that:

$$d = \left\{ \log\left(\rho^a_{m,n}\right); \log\left(M_{m,n,o}\right) \right\}, \tag{11}$$

where the indices vary in the ranges: $m = [1, N_{\text{models}}]$; $n = [1, N_{\text{quads}(m)}]$; $o = [1, N_{\text{gates}(m,n)}]$

The logarithm of the data is usually taken to minimize non-linearity, although this may be omitted to preserve negative decays.

The model is represented by logarithmic parameters for each inversion block, and for the Cole–Cole, parametrization takes the form:

$$\boldsymbol{m} = \left\{ \log\left(\rho_{l,m}\right), \log\left(m_{0l,m}\right), \log\left(\tau_{l,m}\right), \log\left(c_{l,m}\right), \log\left(\mathrm{thk}_{k,m}\right) \right\}, \tag{12}$$

where the indices vary in the ranges: $l = \left[1, N_{\mathrm{layers}}\right]; m = \left[1, N_{\mathrm{models}}\right]; k = \left[1, N_{\mathrm{layers}} - 1\right]$. The use of the logarithm of all the parameters in the inversion algorithm has not been guided by physical considerations, but is a pragmatic solution because our algorithm allows the log transformation on all the parameters or none.

The inverse problem is written as

$$\boldsymbol{G} \cdot \delta\boldsymbol{m} = \delta\boldsymbol{d} + \boldsymbol{e} \tag{13}$$

where $\boldsymbol{G}$ contains the Jacobian and all constraints imposed on the parameters, $\delta\boldsymbol{m}$ is the model update, $\delta\boldsymbol{d}$ is the data and constraints misfit and $\boldsymbol{e}$ contains the observation errors, errors on the constraints and errors on the *a priori* model. The covariance matrix, $\boldsymbol{C}$, for the joint observation error, $\boldsymbol{e}$, can be calculated and the model estimate is obtained as:

$$\delta\boldsymbol{m}_{\mathrm{est}} = \left[\boldsymbol{G}^T \boldsymbol{C}^{-1} \boldsymbol{G}\right]^{-1} \boldsymbol{G}^T \boldsymbol{C}^{-1} \delta\boldsymbol{d} \tag{14}$$

.

This is performed iteratively, minimizing the objective function:

$$Q = \left(\frac{\left[\delta\boldsymbol{d}^T \boldsymbol{C}^{-1} \delta\boldsymbol{d}\right]}{N_{\mathrm{d}} + N_{\mathrm{m}} + N_{\mathrm{R}}} \right)^{\frac{1}{2}}, \tag{15}$$

where N_{d} is the number of data points, N_{m} is the number of model parameters (for *a priori* constraints) and N_{R} is the number of roughness constraints.

For all inversion results the uncertainty analysis for model parameters is computed through the covariance of the estimator error for linear mapping $\boldsymbol{C}_{\mathrm{est}} = \left[\boldsymbol{G}^T \boldsymbol{C}^{-1} \boldsymbol{G}\right]^{-1}$ described by Tarantola & Valette (1982). Because the model parameters are represented as logarithms, the analysis gives a standard deviation factor (STDF) for the ith parameter m_i defined by

$$\mathrm{STDF}\left(m_i\right) = \exp\left(\sqrt{C_{\mathrm{est}(i,i)}}\right). \tag{16}$$

Hence, under a lognormal assumption, it is 68 per cent likely that the ith model parameter m_i falls in the interval

$$\frac{m_i}{\mathrm{STDF}\left(m_i\right)} < m_i < m_i \cdot \mathrm{STDF}\left(m_i\right). \tag{17}$$

In general the STDF contains information on both data and constraints, through $\boldsymbol{G}$ and $\boldsymbol{C}$. This means that the uncertainty computed on the model parameters depends also on the values of roughness constraints and on the prior information. To uncouple the STDF from the constraints, it is possible to propagate through eq. (16) only the data errors. Hereafter the model uncertainty computed only from data errors is referred as uncoupled uncertainty analysis, while the uncertainty analysis that contains both data and constraints information is termed coupled uncertainty analysis. For smooth inversion the $\boldsymbol{G}^T \boldsymbol{C}^{-1} \boldsymbol{G}$ matrix is usually singular, due to the high number of layers, and only the coupled analysis is computed.

EXAMPLES

Two examples of the inversion algorithm are presented in this study, taken from both synthetic and field data. The synthetic example is a three-layer model with lateral variations, which is inverted using the layered model approach. Data for the field example were collected from a landfill site with significant variations in topography and a smooth inversion was applied. For both examples, a gradient array (Dahlin & Zhou 2006) comprising 1250 quadrupoles was used on a profile consisting of 83 electrodes and electrode spacing of 5 m. 20 time gates, of width between 10 and 800 ms, were used for IP measurements, and data were stacked three times with 4 s of current on-time and off-time. In both inversions no *a priori* constraints were imposed, a homogeneous starting model was used and the stopping criterion for the inversion was a relative change in the objective function below 1 per cent.

In the layered inversion of the synthetic data the lateral constraints between adjacent models were set equal to 1.05, and no vertical constraints were imposed between adjacent blocks. This constraint value allows roughly 5 per cent of lateral variation between the constrained parameters. In fact, in the LCI implementation the lateral and vertical constraints represent the relative variation of the parameters (expressed as a factor like in eq. 17) that weights the roughness misfit in the objective function Q through the covariance matrix $\boldsymbol{C}$ of eq. (15). In the smooth inversion of field data different values of the roughness constraints were used. In particular, vertical constraints, equal to 2.0, and lateral constraints, equal to 1.3, were set between the Cole–Cole parameters of adjacent cells. The different values for the roughness constraints for the layered and smooth inversions derive from the different weight of the constraint misfit, compared to the data misfit, in the objective function of eq. (15). In fact, in the layered inversion the number of roughness constraints N_{R} is much smaller than in the smooth inversion, and smaller values for the lateral constraints are needed to obtain smooth models. Thus, in the LCI scheme the trade-off between fitting the data (complex models, no constraints) and fitting the lateral constraints (smooth models, tight constraints) depends also on the ratio

between the number of roughness constraints N_R and the number of data N_d. Numerous experiments on far more complex synthetic models and field data (not shown here) show the proposed settings to be appropriate for a large fraction of layered/smooth models.

Synthetic example

A 2-D TDIP survey was simulated on the three-layer synthetic model of Fig. 4 (sections a2–d2, one for each Cole–Cole parameter), with the sequence settings mentioned earlier. 1 and 10 per cent of Gaussian noise was added to dc and IP data, respectively. Fig. 4, sections (a1)–(d1),
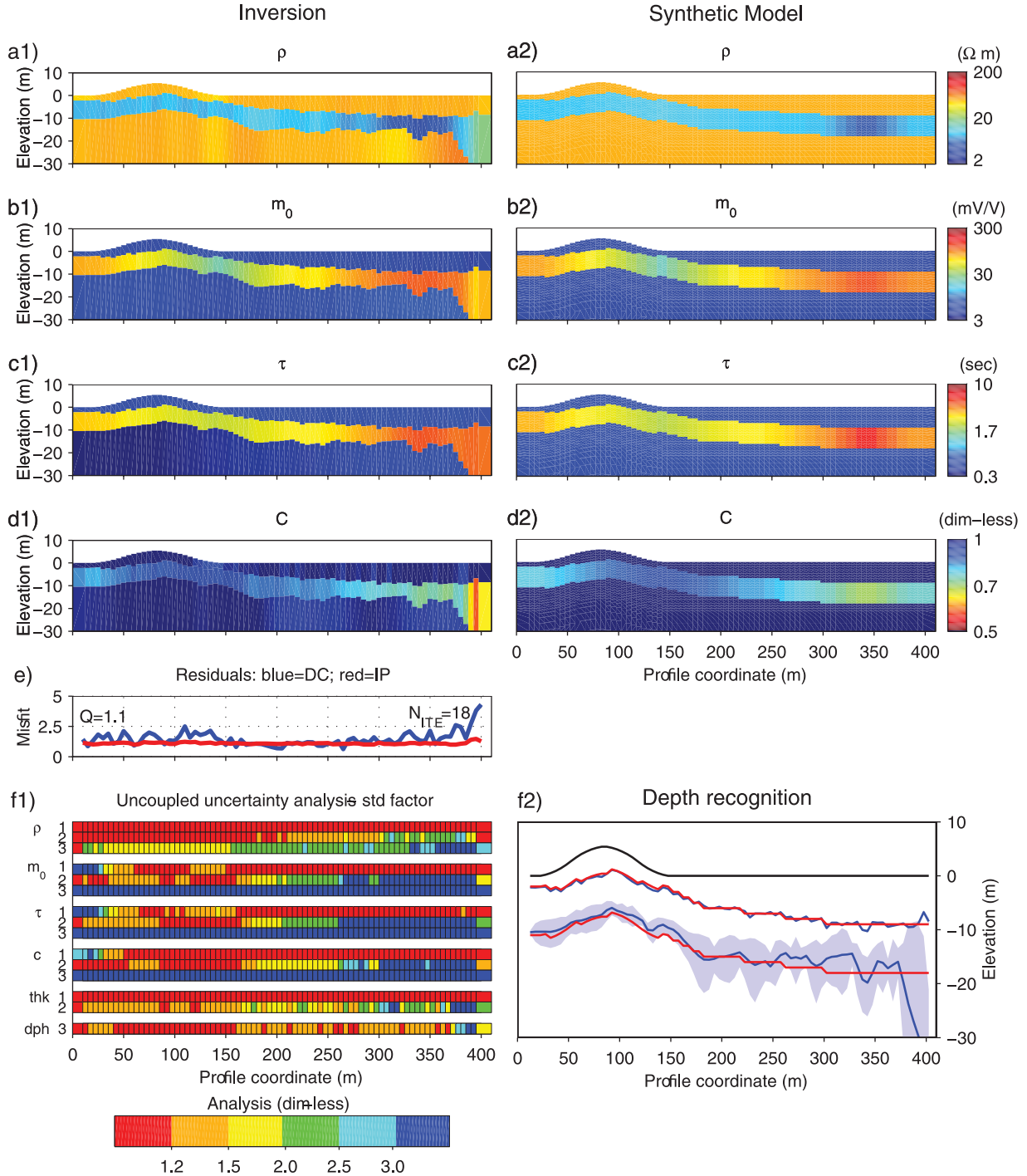
Figure 4. Reconstruction of each model parameter (a1–d1) for the response calculated from a synthetic model (a2–d2). Gaussian noise was added to the forward response for both dc data (1 per cent) and IP data (10 per cent) and a homogenous half-space was used as a starting model. In (e) the data misfit is shown, in terms of eq. (15), for both dc and IP data; (f1) displays the uncoupled uncertainty of each inversion parameter as defined in the inversion section and the uncertainty on the depth to the third layer (dph 3), computed from the thickness uncertainty; (f2) shows the topography (black line) and the depths (red lines) of the synthetic model, together with the inverted depths (blue lines) and the 68 per cent confidence interval (light blue area) as defined in eq. (17).

shows the inversion model. The Cole–Cole parameters and the layer thicknesses are retrieved correctly by the inversion. The lateral variations of all model parameters are properly reconstructed, except at the end of the right-hand side of the profile, where the thickness of the second layer is overestimated.

Fig. 4(e) shows the resistivity and chargeability misfits in two different curves (blue and red, respectively), even if the objective function of the inversion is unique (eq. 15): the resistivity and chargeability data are weighted only through their SD. The dimension-less data misfits in Fig. 4(e) are expressed in terms of eq. (15), by splitting the computations for resistivity and chargeability data and by discarding the constraint misfit. Fig. 4(f1) presents the uncoupled (i.e. computed only from the data uncertainty, and not from the constraints uncertainty) uncertainty analysis on all the inversion parameters, as defined in eq. (16). Fig. 4(f1) shows, together with the uncertainty on the five parameters of the inversion (ρ, m_0, τ, c and thickness thk), the uncertainty of the depth to the third layer, computed by propagating the uncertainty of the thicknesses. It is clear from Fig. 4(f1) that the parameters of the third layer are poorly resolved, as are the IP parameters of the second layer between 260 and 395 m along the profile. In these areas, the lateral constraints help the inversion in retrieving the correct values for the inversion parameters. Fig. 4(f2) presents the depth to the second and to the third layer of the synthetic model (red lines) compared to the depths of the inverted model (blue lines), together with the confidence interval of the inverted depth (light blue areas) as defined in eq. (17). Fig. 4(f2) shows that the depths of the layers are properly retrieved, and the confidence interval, computed only from data errors, give a good estimate of the depth uncertainty. From Figs 4(f1) and (f2) it is also possible to correctly interpret the increase of the thickness of the second layer at the right end of the profile as an inversion artefact. In fact, the thickness and depth uncertainty analysis shows that these parameters are poorly resolved, due to the insufficient coverage of the structure by the electrode array at the end of the profile. In contrast, the end of the left side of the profile is properly reconstructed, because of the shallower depth of the chargeable layer.

Field example

TDIP data gathered from a landfill site at Risby, Copenhagen (Denmark), were chosen to evaluate the inversion algorithm on field data. 10 2-D profiles were gathered crossing the landfill site to delineate the boundaries of the buried waste, of which one is presented here. A comparison with a classical inversion scheme, carried out with the commercial software Res2Dinv (Geotomo Software Inc.), is also presented.

Fig. 5 shows the inversion results (sections a1–d1), together with the data misfit (section e) and the coupled (i.e. computed propagating both data uncertainty and model constraints) uncertainty analysis (sections a2–d2). The dark blue areas of sections (a2)–(d2) correspond to an uncertainty equal or above the lateral constraint value of the inversion, indicating where the parameter retrieval is constraints (and not data) driven. Fig. 6 shows the data misfit in details for the quadrupoles of the acquisition sequence with lateral focus between 245 and 250 m along the profile. Both the apparent resistivity (Fig. 6a) and the chargeability data (Fig. 6b) are well fitted in the entire pseudo-depth range. Borehole data are superimposed on the model sections of Fig. 5 to support the interpretation of the inverted sections and the applicability of spectral parameters. There is very good correspondence between waste layers in each of the four borehole results and high chargeability and c values. This correspondence does not always follow for the resistivity section, highlighting the importance of IP for waste site investigation. The relaxation time (section c1) correlates well with the low resistivity layer (section a1), but the interpretation of this correlation requires further investigation beyond the scope of this paper. In any case it shows that the spectral information retrieved in the inversion reflects physiochemical properties of the soil.

Below the chargeable layer, there is poor resolution of spectral parameters in both the synthetic and field example. This is highlighted by the uncertainty analysis and may be considered analogous to transient electromagnetic methods, where good conductors are well resolved yet may mask the response of deeper resistive layers. Similarly, it appears highly chargeable layers may mask the response of layers below which have a lower IP response. A complete sensitivity analysis for different environments would be required to investigate this problem further, but is beyond the scope of this paper.

Finally a comparison between the 2-D LCI inversion algorithm presented in this study and the Res2Dinv code by Geotomo software (Loke & Barker 1996) is presented in Fig. 7. In Res2Dinv the chargeability is computed in a two-step algorithm by carrying out two dc resistivity forward mapping, for the dc value and for the late time resistivity as described by Oldenburg & Li (1994). The parameters retrieved in the Res2Dinv inversion are the resistivity and the integral chargeability, integrated over the entire range of acquisition of the IP signal. This approach does not take into account the actual waveform used to inject the current (like T_{on}, T_{off} or the number of stacks), or the filter characteristics of the Syscal instrument. Hence, Res2Dinv inversions give different values for the chargeability just by changing the acquisition settings in the field. The Res2Dinv inversion was carried out with smooth constraints and with the vertical to horizontal flatness filter ratio of 0.3 to help the recognition of horizontal structures. The stopping criterion for the inversion was a difference in the data misfit below 1 per cent between consecutive iterations and the final rms misfit was 4 per cent for resistivity and 7 per cent for integral chargeability.

To facilitate the comparison of the two approaches, the integral chargeability was computed also for our inversion scheme, by using the Cole–Cole parameters to calculate the decays and the corresponding values of integral chargeability. Consequently the chargeability sections of Fig. 7 are plotted in the same unit, with the same colour scale.

The 2-D LCI and the Res2Dinv resistivity sections (Fig. 7a) are quite similar in terms of parameter values and anomaly patterns, even if significant differences are present between 50 and 150 m along the profile, at elevations below 10 m. Unfortunately, no resistivity logs are present in the area and the borehole information does not allow to infer what inversion scheme retrieves the best resistivity structure. The chargeability sections (Fig. 7b) show more pronounced discrepancies. The Res2Dinv section presents smaller values of integral chargeability,
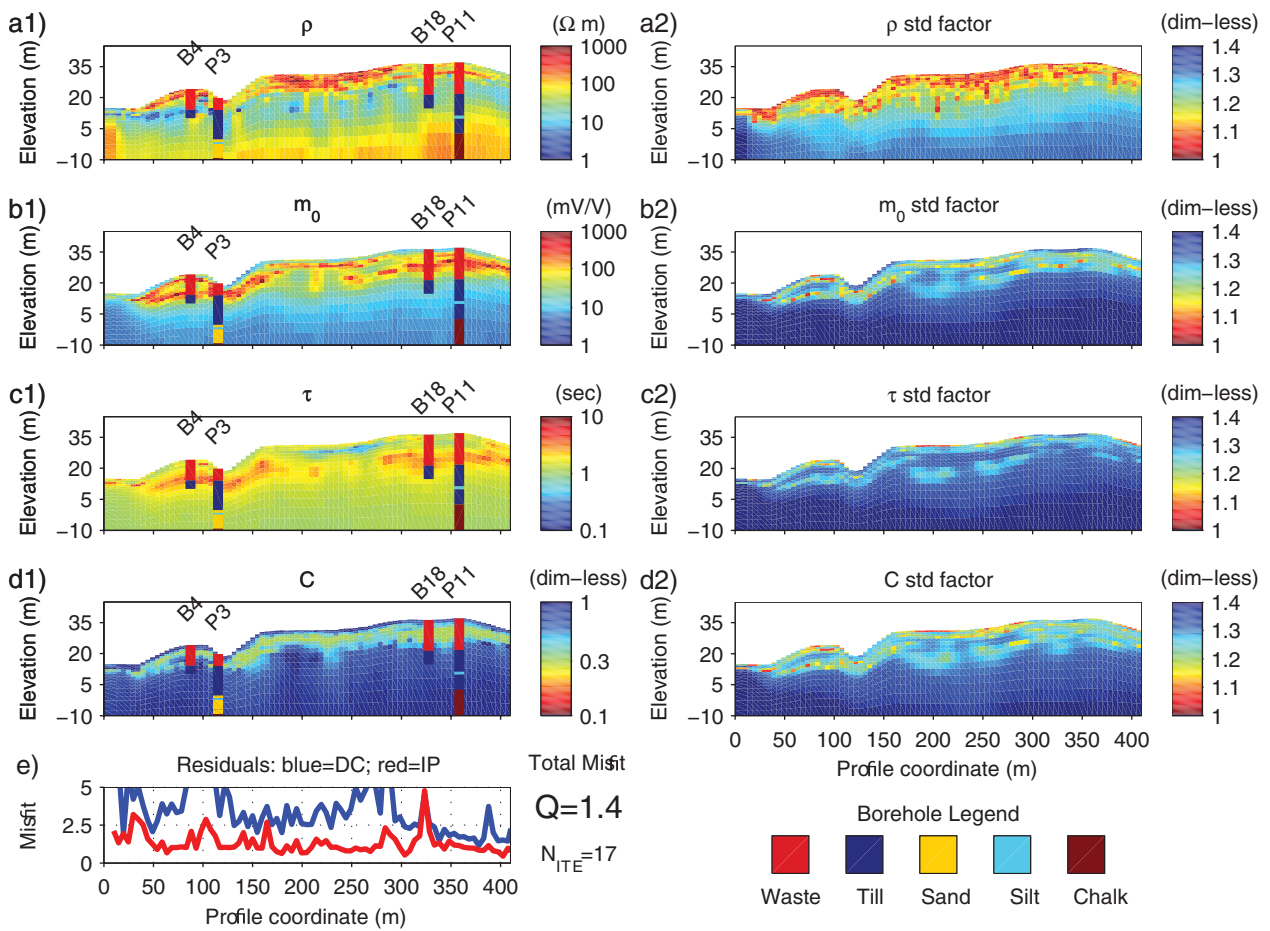
Figure 5. Inversion of data from the Risby field site compared against boreholes. Each model parameter is shown in sections (a1)–(d1), with the corresponding coupled uncertainty in sections (a2)–(d2) as defined in the inversion section. The data misfit, computed in terms of eq. (15) for both dc and IP data, is shown in (e).

with a shallow chargeable area thicker than the 2-D LCI one. The difference in chargeability values derives from the implementation of the current waveform, present only in the 2-D LCI inversion. In fact, the Res2Dinv interpretation uses the step response to model the IP signal, and the retrieved chargeability values are biased when the characteristic IP decay time is comparable to (or greater than) the on/off time of the current injection (Fiandaca *et al.* 2012). When comparing the borehole information with the chargeability sections (Fig. 7b), the correlation between waste deposits and high chargeability is clear in the 2-D LCI inversion. On the contrary, in the Res2Dinv inversion this correlation is not present, except for borehole P11. It has also to be remarked that the integral chargeability sections (Fig. 7b) do not contain any information about the spectral content of the IP data, but the spectral information is present in the 2-D LCI inversion when looking at all the inversion parameters (Fig. 5).

Three minutes per iteration were necessary to perform the 2-D LCI inversion (with five points per decade and MD = 10 electrode spacings) on a 32 core machine (AMD Opteron 6168 CPU, 1.90 GHz), compared to about 16 s per iteration required by the Res2Dinv inversion (with same number of inversion layers and nodes between electrodes). The difference in inversion speed is bigger than the difference shown in Table 1. This is due to the speed of the Res2Dinv forward/Jacobian computations, which is almost twice than the FD forward/Jacobian implementation used in this study. Further improvement of the 2-D LCI inversion speed could be achieved by increasing the speed of the FD forward/Jacobian algorithm, but this is beyond the scope of this study.

CONCLUSIONS

Efficient modelling of TDIP data has been demonstrated. In a new approach, the whole voltage decay is considered and an accurate description of transmitter waveform effects and receiver transfer function is implemented. Spectral parameters, in terms of potentially any spectral model, such as the Cole–Cole model, can be retrieved in a unique inversion process and the examples shown suggest that the information contained in TD data is sufficient to accurately resolve all spectral parameters. Furthermore, optimization of the inversion algorithm allows fast computations, comparable with that of direct current algorithms, which is not at the expense of computational accuracy.

Considering that the transmitter waveform and receiver transfer function have a large impact on the forward response and consequently, on the inverted spectral parameters, it is thought that the improved modelling of TDIP data will help to improve correlation between both
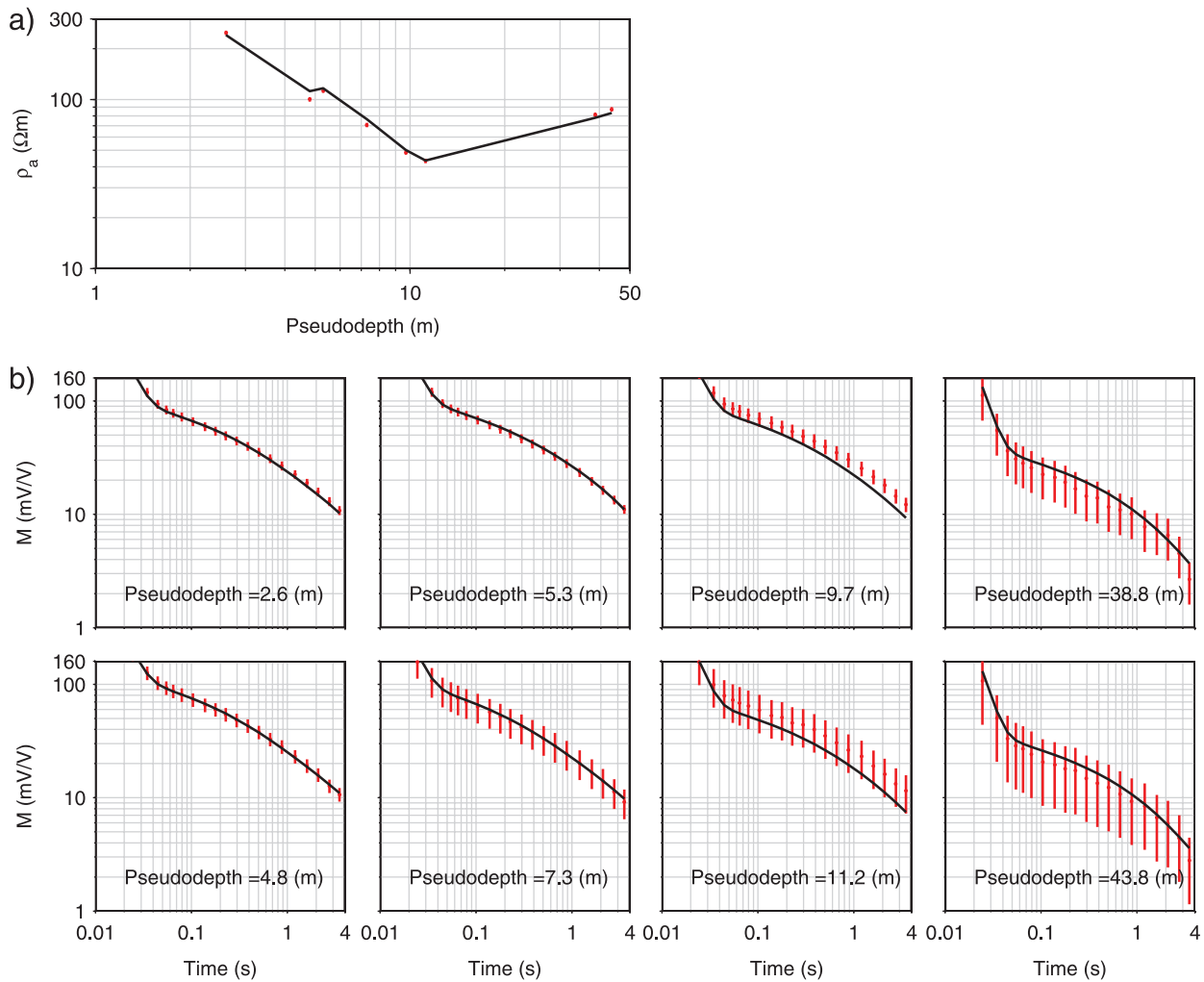
Figure 6. Data fit of Fig. 5 inversion for the quadrupoles of the acquisition sequence with lateral focus between 245 and 250 m along the profile. (a) Apparent resistivity data fit; b) chargeability data fit. Red lines: data with error bars. Black lines: data fit.
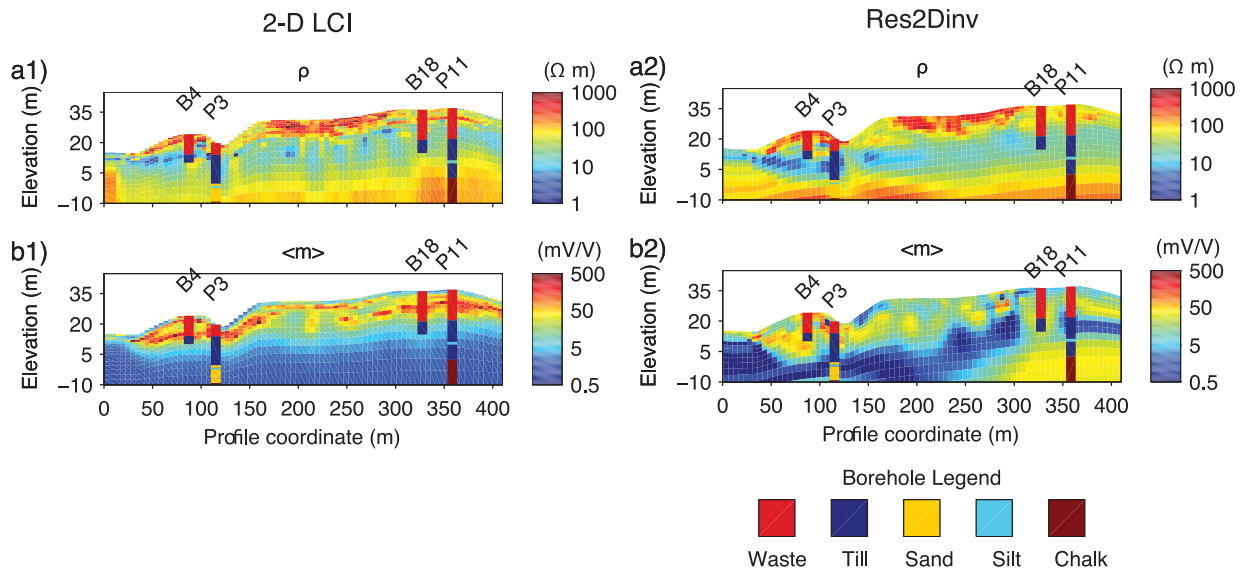
Figure 7. Comparison of 2-D LCI and Res2Dinv inversions, in terms of resistivity and integral chargeability sections. The 2-D LCI integral chargeability section has been derived from the Cole–Cole parameters shown in Fig. 5.

field and laboratory studies, and the TD and FD IP approaches. This is also extremely significant when considering that the majority of field IP surveys are carried out in the TD, while most understanding about links to physical properties comes from laboratory studies performed in frequency domain. The accurate forward modelling and the extraction of spectral information in the inversion process, as described in this paper, could contribute towards changing the applications of TDIP data. Data interpretation could evolve from a qualitative description of the soil, able only to discriminate the presence of contrasts in chargeability parameters, towards a quantitative analysis of the investigated media, which could allow soil-type characterization.

ACKNOWLEDGMENTS

REFERENCES

Aristodemou, E. & Thomas-Betts, A., 2000. DC resistivity and induced polarisation investigations at a waste disposal site and its environments, *J. appl. Geophys.,* **44,** 275–302.

Auken, E. & Christiansen, A.V., 2004. Layered and laterally constrained 2D inversion of resistivity data, *Geophysics,* **69,** 752–761.

Auken, E., Christiansen, A.V., Jacobsen, B.H., Foged, N. & Sørensen, K.I., 2005. Piecewise 1D laterally constrained inversion of resistivity data, *Geophys. Prospect.,* **53,** 497–506.

Auken, E., Christiansen, A.V., Jacobsen, L. & Sørensen, K.I., 2008. A resolution study of buried valleys using laterally constrained inversion of TEM data, *J. appl. Geophys.,* **65,** 10–20.

Behroozmand, A.A., Auken, E., Fiandaca, G. & Christiansen, A.V., 2012. Improvement in MRS parameter estimation by joint and laterally constrained inversion of MRS and TEM data, *Geophysics,* **74,** WB191–WB200.

Binley, A. & Kemna, A., 2005. *DC Resistivity and Induced Polarization Methods,* Springer, Netherlands.

Binley, A., Slater, L.D., Fukes, M. & Cassiani, G., 2005. Relationship between spectral induced polarization and hydraulic properties of saturated and unsaturated sandstone, *Water Resour. Res.,* **41,** 1–13.

Börner, F.D., Schopper, J.R. & Weller, A., 1996. Evaluation of transport and storage properties in the soil and groundwater zone from induced polarization measurements, *Geophys. Prospect.,* **44,** 583–601.

Christiansen, A.V. & Auken, E., 2004. Optimizing a layered and laterally constrained 2D inversion of resistivity data using Broyden's update and 1D derivatives, *J. appl. Geophys.,* **56,** 247–261.

Cole, K.S. & Cole, R.H., 1941. Dispersion and absorption in dielectrics, *J. Chem. Phys.,* **9,** 341–351.

Dahlin, T. & Zhou, B., 2006. Multiple-gradient array measurements for multi-channel 2D resistivity imaging, *Near Surf. Geophys.,* **4,** 113–123.

Dahlin, T., Bernstone, C. & Loke, M.H., 2002. A 3-D resistivity investigation of a contaminated site at Lernacken, Sweden, *Geophysics,* **67,** 1692–1700.

Davidson, D.W. & Cole, R.H., 1951. Dielectric relaxation in glycerol, propylene glycol, and n-propanol, *J. Chem. Phys.,* **19,** 1484–1490.

Effersø, F., Auken, E. & Sørensen, K.I., 1999. Inversion of band-limited TEM responses, *Geophys. Prospect.,* **47,** 551–564.

Fiandaca, G., Auken, E., Gazoty, A. & Christiansen, A.V., 2012. Time-domain induced polarization: full-decay forward modeling and 1D laterally constrained inversion of Cole-Cole parameters, *Geophysics,* **77,** E213–E225.

Flores Orozco, A., Kemna, A., Oberdörster, C., Zschornack, L., Leven, C., Dietrich, P. & Weiss, H., 2012. Delineation of subsurface hydrocarbon contamination at a former hydrogenation plant using spectral induced polarization imaging, *J. Contamin. Hydrol.,* **136–137,** 441–131.

Gazoty, A., Fiandaca, G., Pedersen, J., Auken, E., Christiansen, A.V. & Pedersen, J.K., 2012. Application of time domain induced polarization to the mapping of lithotypes in a landfill site, *Hydrol. Earth Syst. Sci.,* **16,** 1793–1804.

Hönig, M. & Tezkan, B., 2007. 1D and 2D Cole-Cole-inversion of time-domain induced-polarization data, *Geophys. Prospect.,* **55,** 117–133.

Hördt, A., Hanstein, T., Hönig, M. & Neubauer, F.M., 2006. Efficient spectral IP-modelling in the time domain, *J. appl. Geophys.,* **59,** 152–161.

Johansen, H.K. & Sørensen, K.I., 1979. Fast Hankel transforms, *Geophys. Prospect.,* **27,** 876–901.

Johnson, I.M., 1984. Spectral induced polarization parameters as determined through time-domain measurements, *Geophysics,* **49,** 1993–2003.

Kemna, A., Binley, A., Ramirez, A. & Daily, W., 2000. Complex resistivity tomography for environmental applications, *Chem. Eng. J.,* **77,** 11–18.

Kemna, A., Binley, A. & Slater, L., 2004. Crosshole IP imaging for engineering and environmental applications, *Geophysics,* **69,** 97–107.

Loke, M.H. & Barker, R.D., 1996. Rapid least squares inversion of apparent resistivity pseudosections by a quasi-Newton method, *Geophys. Prospect.,* **44,** 131–152.

Oldenburg, D.W. & Li, Y., 1994. Inversion of induced polarization data, *Geophysics,* **59,** 1327–1341.

Pelton, W.H., Ward, S.H., Hallof, P.G., Sill, W.R. & Nelson, P.H., 1978. Mineral discrimination and removal of inductive coupling with multifrequency induced-polarization, *Geophysics,* **43,** 588–609.

Revil, A. & Florsch, N., 2010. Determination of permeability from spectral induced polarization in granular media, *Geophys. J. Int.,* **181,** 1480–1498.

Seigel, H.O., 1959. Mathematical formulation and type curves for induced polarization, *Geophysics,* **24,** 547–565.

Shuey, R.T. & Johnson, M., 1973. On the phenomenology of electrical relaxation in rocks, *Geophysics,* **38,** 37–48.

Slater, L. & Binley, A., 2003. Evaluation of permeable reactive barrier (PRB) integrity using electrical imaging methods, *Geophysics,* **68,** 911–921.

Slater, L.D. & Lesmes, D., 2002. IP interpretation in environmental investigations, *Geophysics,* **67,** 77–88.

Slater, L.D. & Reeve, A., 2002. Investigating Peatland stratigraphy and hydrogeology using integrated electrical geophysics, *Geophysics,* **67,** 365–378.

Tarantola, A. & Valette, B., 1982. Generalized nonlinear inverse problems solved using a least squares criterion, *Rev. Geophys. Space Phys.,* **20,** 219–232.

Titov, K., Tarasov, A., Ilyin, Y., Seleznev, N. & Boyd, A., 2010. Relationships between induced polarization relaxation time and hydraulic properties of sandstone, *Geophys. J. Int.,* **180,** 1095–1106.

Tombs, J.M.C., 1981. The feasibility of making spectral IP measurements in the time domain, *Geoexploration,* **19,** 90–102.

Van Voorhis, G.D., Nelson, P.H. & Drake, T.L., 1973. Complex resistivity spectra of porphyry copper mineralization, *Geophysics,* **38,** 49–60.

Vanhala, H., 1997. Mapping oil-contaminated sand and till with the spectral induced polarization (IP) method, *Geophys. Prospect.,* **45,** 303–326.

Weller, A., Seichter, M. & Kampke, A., 1996. Induced-polarization modelling using complex electrical conductivities, *Geophys. J. Int.,* **127,** 387–398.

Weller, A., Frangos, W. & Seichter, M., 1999. Three-dimensional inversion of induced polarization data from simulated waste, *J. appl. Geophys.,* **41,** 31–47.

Yuval & Oldenburg, D.W., 1997. Computation of Cole-Cole parameters from IP data, *Geophysics,* **62,** 436–448.

APPENDIX: DERIVATION OF THE THICKNESS DERIVATIVE

The LCI scheme requires the computation of thickness derivatives when used for layered inversion. Both in the 1- and 2-D LCI implementations presented so far (Auken & Christiansen 2004; Auken *et al.* 2005, 2008; Behroozmand *et al.* 2012; Fiandaca *et al.* 2012), the derivative computation is done by differentiating two forward responses: the forward response obtained by a small variation of the parameter and the forward response of the unperturbed model space. This approach is a limitation for 2-D implementations, where the forward response is significantly slower, and approximate solutions have been proposed, such as the Broyden update (Christiansen & Auken 2004). To overcome the speed limitation in this work the Jacobian computation for the Cole–Cole parameters is not performed by differentiation, but by manipulating the FD Jacobian obtained with the adjoint method. A method for deriving also the thickness derivative from the adjoint Jacobian is presented here.

Consider, as shown in Fig. A1(a), the forward mesh in the vicinity of the mesh cell singled out by the *i*th and *k*th mesh indices. The variation of the FD forward response ΔF_{FD}^* induced by changing the value of the complex conductivity $\sigma_{i,k}^*$ of the cell$_{i,k}$ to the value $\sigma_{i+1,k}^*$ of the cell$_{i+1,k}$ (Fig. A1b) can be approximated as follows:

$$\Delta F_{\mathrm{FD}}^* \cong J_{i,k}^* \left(\sigma_{i+1,k}^* - \sigma_{i,k}^* \right), \tag{A1}$$

where $J_{i,k}^*$ represents the FD Jacobian of the cell$_{i,k}$ and the expression is exact for infinitesimal differences $\Delta \sigma_{i,k}^* = \left(\sigma_{i+1,k}^* - \sigma_{i,k}^* \right)$.

Fig. A2 presents the sketch of the model space when the variation of complex conductivity $\Delta \sigma_{i,k}^*$ is applied only in the bottom portion of the cell$_{i,k}$, that is equivalent to moving up the boundary between cell$_{i,k}$ and cell$_{i+1,k}$. The difference $\mathrm{d}F_{\mathrm{FD}}^*$ in the forward response between the modified model (Fig. A2b) and the unperturbed model (Fig. A2a) is:

$$\mathrm{d}F_{\mathrm{FD}}^* \cong \mathrm{d}J_{i,k}^* \left(\sigma_{i+1,k}^* - \sigma_{i,k}^* \right), \tag{A2}$$
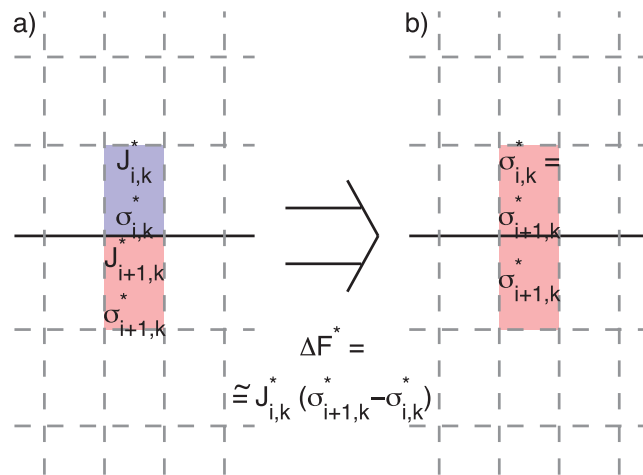

Figure A1. Change in the forward response when varying the complex conductivity of the cell$_{i,k}$. (a) Starting model and (b) perturbed model.
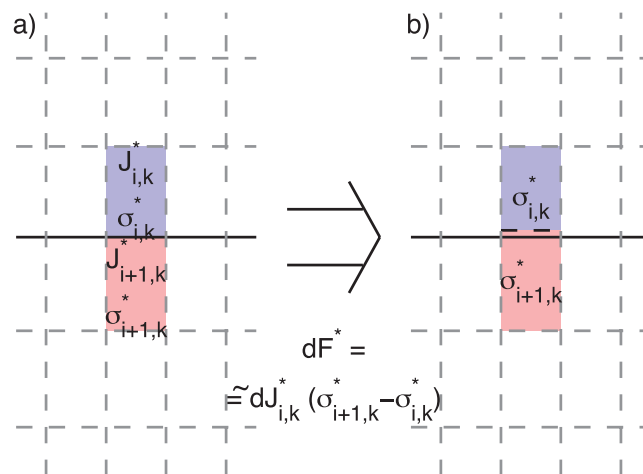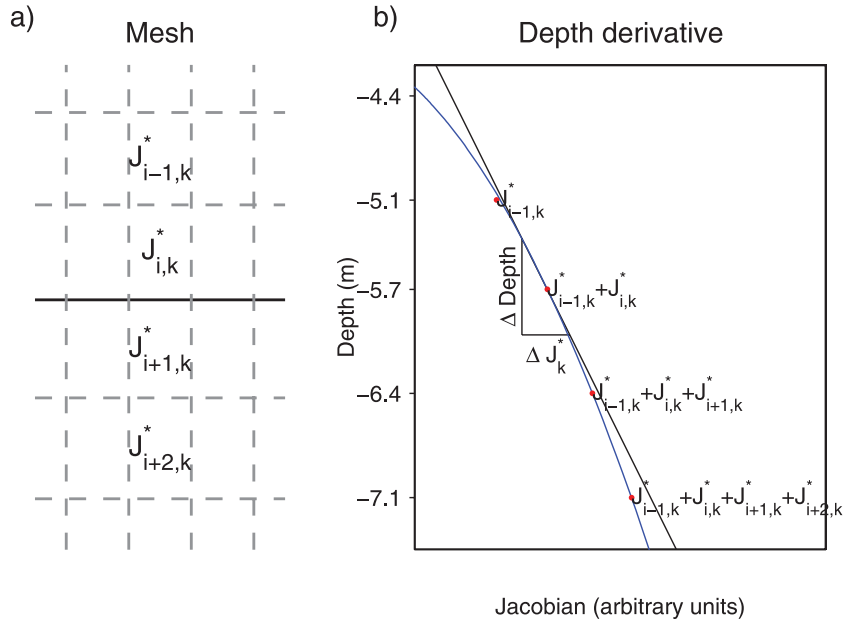

Figure A2. Change in the forward response when moving the boundary between cell$_{i,k}$ and cell$_{i+1,k}$. (a) Starting model and (b) perturbed model.

Figure A3. Calculation of partial derivatives with respect to depth. (a) The mesh discretization and the Jacobian elements $J_{i,k}^* = (\partial F_{\mathrm{FD}}^*/\partial \sigma^*)_{i,k}$, for the mesh cells singled out by the indices i and k. Each element represents the variation of the measurement due to the infinitesimal variation of the complex conductivity of the corresponding cell. (b) Red dots: summation of the Jacobian effect with depth. Blue line: cubic spline fitted between consecutive mesh nodes. Black line and triangle: tangent to the cubic spline, giving $\frac{\partial \left(J_{i,k}^* \right)}{\partial \mathrm{depth}}$.

where $\mathrm{d}J_{i,k}^*$ is the fraction of the Jacobian element $J_{i,k}^*$ corresponding to an infinitesimal horizontal slice of the cell$_{i,k}$, that is,

$$J_{i,k}^* = \int_{\mathrm{depth}_{i-1}}^{\mathrm{depth}_i} \mathrm{d}J_{i,k}^* = \int_{\mathrm{depth}_{i-1}}^{\mathrm{depth}_i} \frac{\partial J_{i,k}^*}{\partial \mathrm{depth}} \mathrm{d}(\mathrm{depth}), \tag{A3}$$

where depth_{i-1} and depth_i represent the depths of the upper and the lower boundaries of the cell$_{i,k}$, respectively.

Following this reasoning, having $\frac{\partial J_{i,k}^*}{\partial \mathrm{depth}}$ is enough to compute the variation in the forward response $\mathrm{d}F_{\mathrm{FD}}^*$ caused by moving the horizontal boundary between cell$_{i,k}$ and cell$_{i+1,k}$. Eq. (A3) can be expanded vertically over several cells by:

$$\sum_{i=j}^{l} J_{i,k}^* = \sum_{i=j}^{l} \int_{\mathrm{depth}_{i-1}}^{\mathrm{depth}_i} \mathrm{d}J_{i,k}^* = \sum_{i=j}^{l} \int_{\mathrm{depth}_{i-1}}^{\mathrm{depth}_i} \frac{\partial J_{i,k}^*}{\partial \mathrm{depth}} \mathrm{d}(\mathrm{depth}) = \int_{\mathrm{depth}_{j-1}}^{\mathrm{depth}_l} \frac{\partial J_k^*}{\partial \mathrm{depth}} \mathrm{d}(\mathrm{depth}). \tag{A4}$$

Under the assumption that $\frac{\partial J_k^*}{\partial \mathrm{depth}}$ is continuous through the cell boundaries (strictly true for infinitesimal differences $\Delta \sigma_{i,k}^*$), the function $\frac{\partial J_k^*}{\partial \mathrm{depth}}$ can be computed by differentiating analytically the cubic spline that fits four consecutive values of $\sum_{i=j}^{l} J_{i,k}^*$ (Fig. A3).

Consequently the ratio between the forward variation $\mathrm{d}F_{\mathrm{FD}}^*$ and the infinitesimal variation of the boundary depth$_i$ between cell$_{i,k}$ and cell$_{i+1,k}$, that is, the depth derivative of the forward response, can be written as:

$$\frac{\partial F_{\mathrm{FD}}^*}{\partial \mathrm{depth}_i} \cong \left. \frac{\partial J_k^*}{\partial \mathrm{depth}} \right|_{\mathrm{depth}=\mathrm{depth}_i} \Delta \sigma_{i,k}^*. \tag{A5}$$

The thicknesses of the cells, and not their depths, are the model parameters in the LCI scheme. Fig. A4 shows the difference in the model variation when changing the depth of the boundary between cell$_{i,k}$ and cell$_{i+1,k}$ (Fig. A4a) and the thickness thk$_i$ of cell$_{i,k}$ (Fig. A4b). It follows that the depth and thickness derivatives are linked through the equation:

$$\frac{\partial F_{\mathrm{FD}}^*}{\partial \mathrm{thk}_n} = \sum_{i=n}^{N_{\mathrm{Layers}}-1} \frac{\partial F_{\mathrm{FD}}^*}{\partial \mathrm{depth}_i}. \tag{A6}$$

Finally the time domain thickness derivative is obtained by applying the same linear transformation used for the forward response. Eq. (A5) is exact for infinitesimal values of $\Delta \sigma^*$, while in practice the error is typically 10–20 per cent, as shown in main body of the paper. However, the derivation of the thickness derivative proposed here is general and gives significant advantages in terms of computational speed when applied to finite element codes in which the Jacobian is computed through the adjoint method.

a)   Model update
     by modifing
     depth$_{i,k}$

b)   Model update
     by modifing
     thickness$_{i,k}$
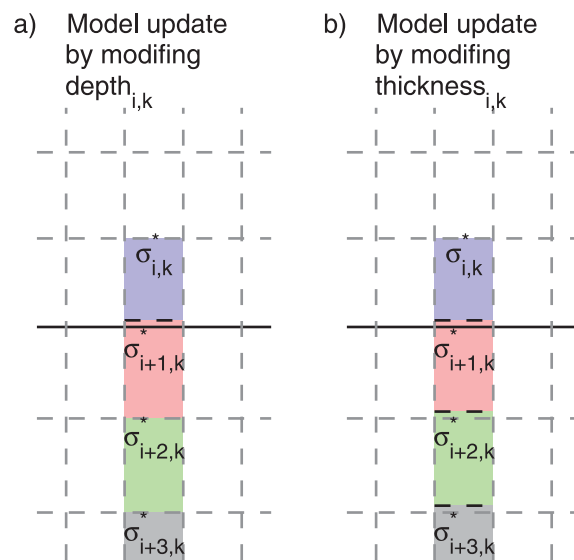
Figure A4. (a) Model update by varying the boundary between the cell$_{i,k}$ and the cell$_{i+1,k}$. (b) Model update by varying the thickness of the cell$_{i,k}$.